UC Berkeley
UC Berkeley Previously Published Works

Title

The ^{40}Ar(d,p)^{41}Ar cross section between 3-7 MeV.

Permalink

https://escholarship.org/uc/item/4f07113w

Authors

Bleuel, DL
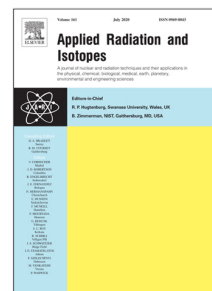Anderson, SG
Bernstein, LA
et al.

Publication Date

2022-12-01

DOI

10.1016/j.apradiso.2022.110509

Peer reviewed

Journal Pre-proof

The ^{40}Ar(d,p)^{41}Ar cross section between 3–7 MeV

D.L. Bleuel, S.G. Anderson, L.A. Bernstein, J.A. Brown,
J.A. Caggiano, B.L. Goldblum, J.M. Gordon, J.M. Hall, K.P. Harrig,
M.S. Johnson, T.A. Laplace, R.A. Marsh, M.E. Montague,
A. Ratkiewicz, B. Rusnak, C.A. Velsko

Please cite this article as: D.L. Bleuel, S.G. Anderson, L.A. Bernstein et al., The ^{40}Ar(d,p)^{41}Ar cross section between 3–7 MeV. *Applied Radiation and Isotopes* (2022), doi: https://doi.org/10.1016/j.apradiso.2022.110509.

This is a PDF file of an article that has undergone enhancements after acceptance, such as the addition of a cover page and metadata, and formatting for readability, but it is not yet the definitive version of record. This version will undergo additional copyediting, typesetting and review before it is published in its final form, but we are providing this version to give early visibility of the article. Please note that, during the production process, errors may be discovered which could affect the content, and all legal disclaimers that apply to the journal pertain.

The ^{40}Ar(d,p)^{41}Ar cross section between 3-7 MeV

D. L. Bleuel[a], S. G. Anderson[a], L. A. Bernstein[b,c], J. A. Brown[b], J. A. Caggiano[a], B. L. Goldblum[c,b], J. M. Gordon[b], J. M. Hall[a], K. P. Harrig[b], M. S. Johnson[c], T. A. Laplace[b], R. A. Marsh[a], M. E. Montague[b], A. Ratkiewicz[a], B. Rusnak[a], C. A. Velsko[a]

[a]*Lawrence Livermore National Laboratory, Nuclear and Chemical Sciences Division, Livermore, California 94550, USA*
[b]*University of California, Department of Nuclear Engineering, Berkeley, California 94720, USA*
[c]*Lawrence Berkeley National Laboratory, Nuclear Science Division, Berkeley, California 94720, USA*

Abstract

To determine the safety of using argon as a deuteron beam stopping material, the ^{40}Ar(d,p)^{41}Ar cross section was measured at average deuteron energies of 3.6 MeV, 5.5 MeV, and 7.0 MeV using an activation method. A 16-MeV deuteron beam produced by Lawrence Berkeley National Laboratory's 88-Inch Cyclotron was degraded to each energy by nickel foils and the front wall of an aluminum gas chamber. The reduced-energy deuterons were used to activate a sample of ^{nat}Ar gas. After each irradiation, the gas chamber's ^{41}Ar activation was measured with a high-purity germanium detector. The cross sections measured were larger than a previous measurement by ∼40%.

Keywords: argon cross section γ ray activation

1. Introduction

A high-intensity neutron source, depicted in Fig. 1 using a windowless gas target (Johnson et al., 2017), is being constructed at Lawrence Livermore National Laboratory (LLNL) to perform neutron imaging (NI). Two accelerators capable of delivering a beam of 4 MeV or 7 MeV deuterons to a deuterium-filled, windowless gas cell, will produce quasi-monoenergetic beams of, respectively, 7 MeV or 10 MeV in the forward direction by D-D fusion. The high instantaneous beam current of 25 mA (300 μA average) and narrow spatial focus necessitates the windowless gas design, as the beam would quickly melt or ablate solid materials. A beam of narrow energy spread (∼250 keV) can be achieved by a thin areal density (∼0.72 mg/cm^2) chamber of deuterium gas followed by a beam-stopping volume of another gas with

Figure 2: (Color online) Schematic of LLNL's neutron imaging facility gas cell design, in which a 4 MeV or 7 MeV deuteron beam traverses (a) a deuterium gas volume, a mixing volume between, and (b) a beam-stopping volume of argon or another gas. Red and blue arrows indicate gas flow.

low neutron production, shown in Fig. 2. The original point design for the beam-stopping volume was argon. However, it was estimated that the use of argon could produce a significant radiation hazard from the buildup of ^{41}Ar via the ^{40}Ar(d,p)^{41}Ar reaction. As only a single measurement (Engle et al., 2012) had previously been made at energies below 7 MeV and in an experimental configuration optimized for a different measurement (of ^{38}Cl production), we measured the ^{40}Ar(d,p)^{41}Ar cross section using an activation technique.
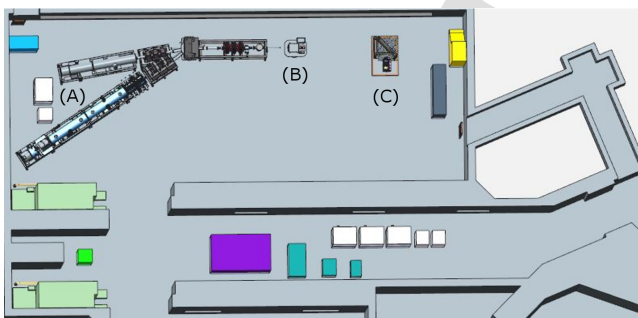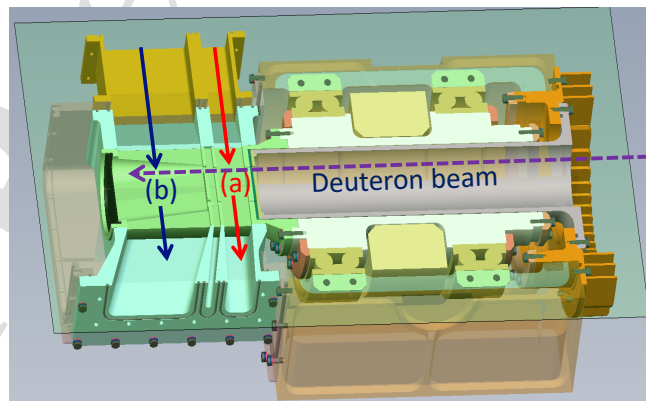

Figure 1: (Color online) Schematic of LLNL's neutron imaging facility with (A) 4 MeV (top) and 7 MeV (bottom) accelerators, (B) gas target, and (C) imaging station.

2. Experimental setup

Experiments were performed at Lawrence Berkeley National Laboratory's 88-Inch Cyclotron. A previous measurement (Engle et al., 2012) suggests that the ^{40}Ar(d,p)^{41}Ar reaction cross section does not change significantly over a large range of deuteron energies below 7 MeV. Furthermore, there is a significant ($\sim$1-2%) uncertainty in the beam energy supplied by the 88-Inch Cyclotron. Thus the experiment was optimized for accuracy in cross section measurement but not in deuteron energy. Two gas containers, similar to those used at the National Ignition Facility (Ratkiewicz et al., 2016), shown in Fig. 3, were evacuated, weighed four times on a high-precision scale, then filled with $\sim$1 atm of natural argon gas and weighed an additional four times. The abundance of ^{40}Ar in natural argon is 99.6035(25)% (Nuclear Wallet Cards, September 2019). The mass of argon in each cell was determined both by the weight difference as well as calculated from the measured pressure, temperature, and volume of the cell, assuming the ideal gas law. Each method of determining these masses, shown in Tab. 1, agreed within 1σ of their uncertainties.
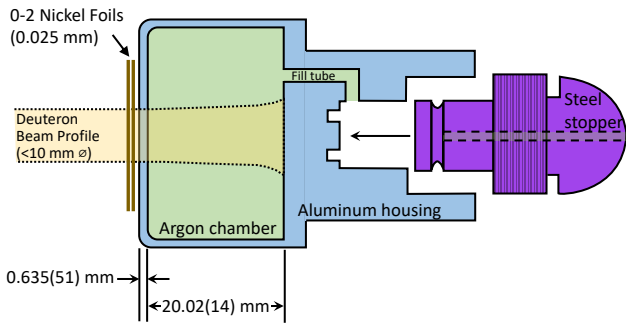

Figure 3: (Color online) Schematic of capsule containing natural argon gas. The beam angular spread and fill tube diameter are not to scale and considerably exaggerated.

Table 1: Masses of natural argon in two gas capsules as determined by cell weight before and after filling and calculated from gas properties (indicated), assuming the ideal gas law (IGL).

Property	Capsule A	Capsule B
Weight with vacuum	95.5009(2) g	94.7952(2) g
Weight with argon	95.5341(2) g	94.8280(3) g
Gas pressure	766.82 torr	767.55 torr
Gas temperature	22.00 C	22.05 C
Capsule volume	19.81(11) cm^3	19.81(11) cm^3
Mass of argon in cell	33.2(3) mg	32.8(4) mg
IGL-calculated mass	33.0(3) mg	33.0(3) mg

Each gas capsule was mounted at the end of a 2 m beam pipe extension off the end of a beam box in the Cave 0 experimental end station at the 88-Inch Cyclotron.

This beam pipe extension was electrically isolated from the beam box and rest of the beam line such that the current from the deuteron beam could be monitored. A permanent magnet was installed between this long, isolated pipe and the upstream beam box to deflect delta electrons, liberated from the beam striking the capsule, to minimize loss of charge.

Before irradiation of each capsule, Gafchromic film was exposed to the focused deuteron beam at three locations, equivalent to the front face of the gas, the end of the gas chamber, and the back of the beam pipe. This ensured in each experiment that the beam spot radius was less than 0.5 cm, thus avoiding striking the small fill tube channel, offset from the beam axis by 1 cm. Equally-sized and positioned beam profiles on each of the three films indicated the beam was parallel.

Nickel foils, indicated in Fig. 3, were mounted on the front face of the gas chambers in three of four measurements, both to degrade the beam energy and act as a fluence monitor. The four measurements were performed in two sessions, separated significantly enough in time (14.5 h) to allow for decay of 99.6% of the ^{41}Ar generated from the previous measurement. The current was also increased in the second session by a factor of three so that the subtraction of this residual activation was only $\sim$0.1%. In both sessions, however, the beam current was kept low enough to avoid heating or columnar ionization of the gas, which could reduce the areal density traversed by the beam. A common energy (corresponding to degradation by a single nickel foil in addition to the aluminum window) was measured between the two sessions as a consistency check. The two different beam currents used in this consistency check confirmed no current-dependent heating or ionization occurred. These parameters are summarized in Tab. 2. The systematic uncertainty in the average deuteron energy through the argon gas due to both the original beam energy uncertainty and uncertainty in the aluminum front face thickness is noted separately from the distribution around the mean energy following attenuation through the nickel, aluminum, and argon. The details of how these parameters are calculated are discussed in the following sections.

Following each irradiation, the activation of the gas capsules and nickel attenuators were each measured at a distance of 12.2 cm from the same upwards-facing high-purity germanium (HPGe) detector. The gas capsules were oriented with the front face (left side of Fig. 3) facing the HPGe detector. This HPGe detector and sample were enclosed in a lead box 20 cm thick to reduce environmental background.

3. Methods

3.1. Energy uncertainties and angular spread

The experiment was dominated by two major sources of systematic energy uncertainty, originating from the uncertainty in deuteron beam energy provided by the cyclotron

Table 2: Configuration details from four measurements.

Quantity	Exp. 1	Exp. 2	Exp. 3	Exp. 4
Beam energy (MeV)	16.00(16)	16.00(16)	16.00(16)	16.00(16)
Gas Capsule	A	B	B	A
Number of Ni foils	1	2	1	0
Time (s)	600(1)	600(1)	600(1)	600(1)
Charge measured on target (μC)	4.32(2)	4.24(2)	13.44(6)	13.68(6)
Charge calculated from 283 keV nickel activation (μC)	4.60	4.36	13.76	–
Charge calculated from 656 keV nickel activation (μC)	4.49	4.30	14.05	–
Avg. current (nA)	7.20(4)	7.07(4)	22.4(1)	22.8(1)
E_{avg} in argon (MeV)	5.5(5)	3.6(7)	5.5(5)	7.0(5)
Energy spread (MeV)	0.25	0.33	0.25	0.20

and the significant aluminum front wall thickness of the gas capsule. Furthermore, the beam energy distribution broadens significantly through this aluminum layer and in the gas itself. This energy broadening was considered separately from the systematic uncertainties, which affect the mean value of the distribution.

3.1.1. Energy and angular straggle

The beam energy spread from charged particle straggling, as well as the distribution in path lengths, was calculated using the Monte Carlo code TRIM, part of the SRIM stopping-power code package (Ziegler et al., 2010). These simulations were also used to ensure that the expected angular spread (depicted in Fig. 3) of a 1 cm diameter beam would not cause deuterons to enter the offset argon fill tube.

Twenty TRIM geometries were simulated for a nominal 16.0 MeV deuteron beam with 0, 1 or 2 nickel attenuators, a 0.635 mm aluminum gas capsule surface, and increasing thicknesses of argon gas volumes from 0.5 to 19.5 mm in 0.1 mm intervals. The energy spectra exiting each of these twenty volumes was then added together to produce a representation of the average energy throughout the entire volume. This average spectrum, along with the contribution from the first and last simulation (each of which contribute 1/20th to the average), is shown in Fig. 4 for each experiment with 0, 1, or 2 nickel attenuators in front of the aluminum. The means of these distributions are listed in Tab. 2 along with the energy spread, which are one standard deviation of each of these approximately-Gaussian distributions.

For the experiment with two nickel attenuators (Exp. 2), the average deflection off axis of deuterons entering the gas cell is only 0.05 mm. The average radial deflection exiting the gas cell is 1.5 mm, adding 0.11 mm to the average path length, or 0.57%. Areal densities in each experiment were adjusted by these factors, which were 0.36% for Exp. 1 and 3 and 0.26% for Exp. 4.

3.1.2. Beam Energy Uncertainty

A substantial uncertainty in the deuteron beam energy delivered by the cyclotron was estimated (Ninemire, 2016)
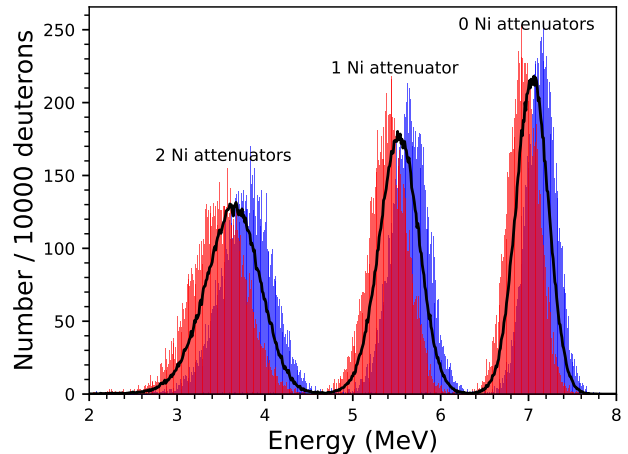

Figure 4: (Color online) Deuteron energy spectra (black) through 20 mm argon gas volume after 0, 1, or 2 nickel attenuators and a 0.635 mm aluminum surface, from the average of twenty distributions in 0.1 mm thick volumes. The first (blue) and last (orange) cell energy distributions are also shown, with the overlap region in dark red.

as 1σ=1%, or $\pm$160 keV. To determine the uncertainty in the final mean deuteron energy in the argon gas, TRIM simulations were also performed for each of the three geometries with an incident particle energy of 16.16 MeV and 15.84 MeV.

The stopping power, and therefore the mean energy, is mostly linear through the relatively-thin argon areal density. With this assumption, the mean can be estimated as simply the average of the mean energy of the first cell and the last cell. In fact, for the three cases shown in Fig. 4, the means calculated in this fashion are within 0.05% as that calculated from averaging twenty volumes, while the standard deviation differs by 4% or less. For uncertainties calculated in this section and Sec. 3.1.3, in which only the change in mean energy is considered, the full twenty volumes were not simulated. Instead, the average of the argon entrance and exit mean energies was used.

The energy uncertainties for Exp. 1-4 from this proce-

3

dure were, respectively, 450, 470, 450, and 300 keV (naturally, Exp. 1 and 3 are identical). These values did not vary significantly (generally less than 5%) between the higher and lower bounds and, given the large magnitude and broader assumptions made in their generation, the positive and negative uncertainties were simply averaged rather than reported separately.

3.1.3. Energy Uncertainty from Aluminum Thickness

An 8% reported manufacturing tolerance in the thickness of the aluminum gas cell wall led to a considerable uncertainty in the energy loss through this layer. It was assumed that this tolerance represents a 3σ uncertainty (i.e., fewer than 0.3% of manufactured parts fall outside the tolerance interval) and for uncertainty analysis, the 1σ uncertainty in thickness was set at 2.7%, or ±0.017 mm.

Similar to the beam energy uncertainty calculations described in Sec. 3.1.2, TRIM simulations were performed for a ±0.017 mm aluminum thickness for each configuration of nickel foils and the effect on the mean energy was determined from the average of the entrance and exit distributions. The energy uncertainties for Exp. 1-4 from this procedure were, respectively, 400, 530, 400, and 340 keV.

As the aluminum thickness and beam energy uncertainties were uncorrelated and dominated all other contributions to energy uncertainties, they were added in quadrature to obtain the total systematic energy uncertainty in Tab. 2. This is reported separately from the energy spread described in Sec. 3.1.1, which was found to be largely independent of each of these perturbations.

3.2. Detector Calibration

An energy-dependent calibration of the HPGe detector was obtained using a well-characterized 0.71 μCi sealed source, ^{152}Eu, shown in Fig. 5 for one particular distance (12.2 cm) from the detector. Measurements of a 0.37 μCi ^{60}Co source are also shown for corroboration, though not used for calibration to avoid systematic activity uncertainties from potentially introducing fit fluctuations.

The Fitzpeaks (Fitzpeaks, 2016) code was used for all γ-ray photopeak fitting, while a custom python routine using a non-linear least squares fit function was written to interpolate photopeak detection efficiency, $\epsilon(E_\gamma)$, between the 11 strongest measured γ-ray emissions of ^{152}Eu, using the formula (Knoll, 1989),

$$\ln \epsilon(E_\gamma) = \sum_{i=0}^{4} a_i \ln(E_\gamma)^i, \quad (1)$$

where a_i are fit parameters and E_γ is the γ-ray energy.

Two uncertainties associated with this functional fit procedure were calculated. Calculation of a systematic "interpolation error" of 1.24%, from the accuracy of interpolating with Eq. 1, is fully described in Bleuel et al. (2021). Additionally, a "fit variability" uncertainty, due to the statistical uncertainties of the measured ^{152}Eu and
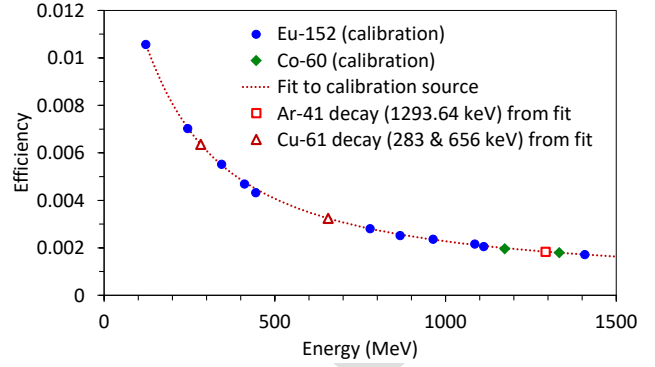

Figure 5: HPGe detector energy-dependent calibration 12.2 cm from the detector, including measured efficiencies from sealed sources (closed datapoints) and interpolated efficiencies of characteristic γ rays from products of argon and nickel reactions with deuterons (open datapoints). Error bars are smaller than the datapoints.
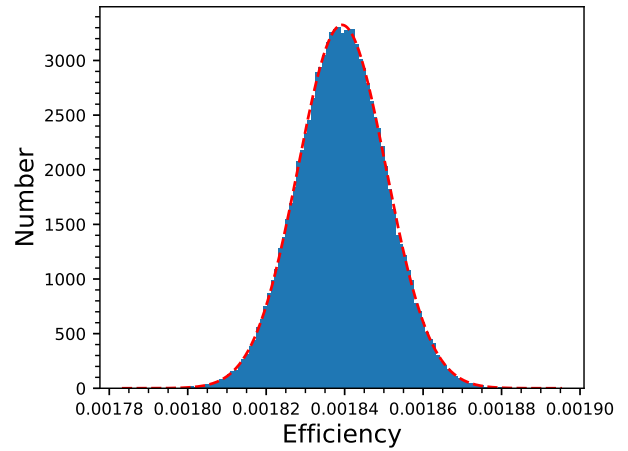

Figure 6: (Color online) Histogram of the 1293.65 keV γ-ray detection efficiency as determined using Monte Carlo sampling of the statistical uncertainty using 100,000 trials.

^{60}Co γ rays, was calculated by a Monte Carlo method, refitting 100,000 perturbed efficiency curves. Each peak activity for the calibration source was sampled from a normal distribution about its measured value with width characterized by its peak integral uncertainty. The distribution of the interpolated efficiencies of the 1293.64 keV γ-ray emission from ^{41}Ar decay from these perturbed fits is shown in Fig. 6. The standard deviation from these interpolated efficiencies was 1.01%.

In addition, an uncertainty of 1.16%, provided by the manufacturer, was ascribed to the absolute activity of the calibration source. These three uncertainties were added in quadature to determine a total calibration uncertainty at 1293.64 keV of 1.88%, for a centered point source 12.2 cm from the detector.

However, the argon gas constituted a volumetrically-distributed source: a cylinder 3.594(5) cm in diameter and 2.002(14) cm tall. To calculate the average efficiency over
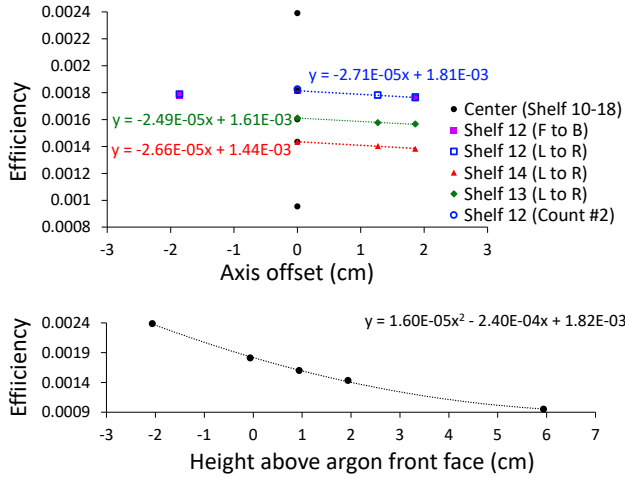
Figure 7: (Color online) Efficiency of the HPGe detector at 1293.64 keV as a function of the offset from center (top) for different detector heights and the horizontal axes (Front to Back or Left to Right), and at the center as a function of height (bottom).

this volume, the ^{152}Eu source was measured at a number of representative positions and heights from the detector, as shown in Fig. 7. Each shelf indicated is 2 mm higher than the shelf number in centimeters (e.g. Shelf 12 is at 12.2 cm from the detector). The center of Shelf 12 was measured twice on two different days to confirm repeatability.

Linear and quadratic functions, shown as dotted lines, were found to fit the data well, within ~1% of all measurements, respectively as a function of radial distance and height. The radial measurements also showed extremely consistent symmetry across both orthogonal horizontal axes, indicated as (F to B) for "front to back," and (L to R) for "left to right." From all these measurements, a single equation could be fit to determine the efficiency at any point in the argon gas volume,

$$\epsilon(R, z) = c_0 R + c_1 z^2 + c_2 z + c_3, \tag{2}$$

where the fit parameters, c_i are given in Tab. 3, R is the radius off axis, and z is the height relative to the bottom of the argon volume (which is 0.635 mm higher than Shelf 12 due to the aluminum container).

Table 3: Fit parameters to Eq. 2.

Parameter	Value
c_0	-2.687×10^{-5}
c_1	1.598×10^{-5}
c_2	-2.400×10^{-4}
c_3	1.819×10^{-3}

While the maximum deviation of any measured point to this equation was 1.2% (which is partially encompassed by the fit variability uncertainty), the assumed uncertainty due to the incompleteness of characterization of the entire volume from a limited number of measurements was con-

servatively set higher at 2%.

Then the volumetric integral over the height of the argon chamber, H, and radius, R_0, gives the total efficiency, ϵ_V:

$$\begin{aligned}
\epsilon_V &= \frac{2\pi}{\pi R_0^2 H} \int_0^{R_0} \int_0^H \epsilon(R, z) R dz dR \\
&= \frac{2}{3} c_0 R_0 + \frac{1}{3} c_1 H^2 + \frac{1}{2} c_2 H + c_3.
\end{aligned} \tag{3}$$

Using the parameters in Tab. 3, a radius of 1.80 cm, and a height of 2.002 cm, this equates to 0.00157.

Furthermore, the front face of the 0.635(5) mm thick aluminum capsule attenuated γ rays. To determine the reduction in efficiency due to this attenuation, a 1-mm-thick sheet of aluminum was placed underneath a ^{152}Eu point source and measured. This reduced the efficiency by 1.2%. Assuming exponential attenuation with thickness, the effect of 0.635 mm of aluminum was calculated to be a 0.77% reduction, to ϵ_V=0.00156.

A summary of the uncertainties and their quadrature sum is listed in Tab. 4.

Table 4: Uncertainties (all 1σ) in ϵ_V (1293.64 keV) determination from point calibration sources.

Uncertainty	Relative value
Interpolation error	1.24%
Fit variability	1.01%
Sealed source activity	1.16%
Volumetric integral	2.%
Aluminum Attenuation	<0.1%
Total	3.4%

3.3. Nickel attenuators and beam monitors

Thin, natural-abundance nickel foils were used as beam degraders as well as integrated current monitors, as a consistency check on the integrated charge collection. The ^{nat}Ni(d,x)^{61}Cu is an IAEA-standard monitor reaction for medical and industrial applications (Hermanne et al., 2018). This reaction was considered best suited for this experiment as the cross section, shown in Fig. 8, was both thought to be well known and does not change dramatically as a function of energy around 16 MeV, the incident beam energy.

Exp. 1 and 3 included a single nickel attenuator while Exp. 2 included two. After each irradiation, activation of the beam-facing nickel foil was measured in an HPGe detector. The two primary γ rays emitted from the decay of ^{61}Cu are 283 keV and 656 keV, with intensities, $\mathscr{I}_\gamma$, respectively, of 12.2% and 10.8% according to the Nuclear Data Sheets (Zuber and Singh, 2015). The activated nickel foils, counted 12.2 cm from the detector front face, were assumed to be point sources, and the efficiencies for the emitted γ rays from ^{61}Cu were interpolated using the curve fit shown in Fig. 5.
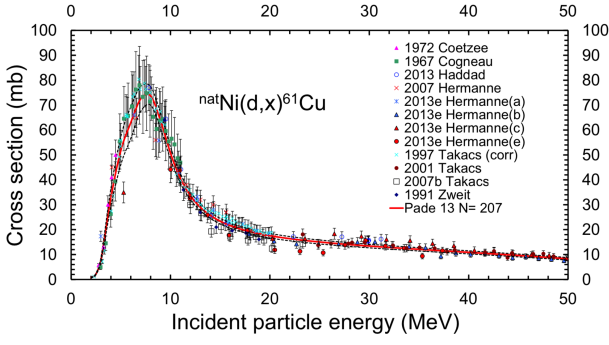
5

Figure 8: (Color online) Experimental and evaluated cross sections for the ^{nat}Ni(d,x)^{61}Cu reaction from Hermanne et al. (2018).

The integral of the beam current, Q, is calculated from the number of counts, C, of each of these characteristic γ rays detected by:

$$Q = \frac{C\lambda A_{Ni}q_d\Delta t_i e^{\lambda\Delta t_{dk}}}{\rho_{Ni}N_A\sigma\epsilon(E_\gamma)f_\ell\mathscr{I}_\gamma(1-e^{-\lambda\Delta t_c})(1-e^{-\lambda\Delta t_i})}, \quad (4)$$

where λ is the decay constant of ^{61}Cu, A_{Ni} is the atomic weight of natural nickel, q_d is the charge per deuteron (1.602 x 10^{-19} C), Δt_i is the irradiation time, ρ_{Ni} is the areal density of the nickel foil in g/cm^2, N_A is Avogadro's number, σ is the cross section of the ^{nat}Ni(d,x)^{61}Cu reaction at the average deuteron energy (15.6 MeV) in each beam-facing nickel foil, $\epsilon(E_\gamma)$ is the efficiency of the HPGe detector to detect the characteristic γ ray of energy E_γ, f_ℓ is the detector live time fraction, Δt_c is the time over which the foils were counted, and Δt_{dk} is the time elapsed between the end of the experiment and the start of the count. The beam current was relatively constant over the short (10 minute) irradiation times, making second-order in-beam decay corrections negligible.

Calculations of the charge varied significantly and consistently in each foil depending on which characteristic γ-ray emission was measured. This led to a comprehensive investigation (Bleuel et al., 2021) of the published intensities of ^{61}Cu γ-ray emissions, in which it was discovered that the ratio of the 656 keV intensity to that at 283 keV in the Nuclear Data Sheets was incorrect by 11%. Although only ratios of intensities, not absolute values, were measured, consistency amongst eleven other γ-ray emissions in over a hundred measurements strongly indicates that the 656 keV γ-ray intensity was in error, with a more accurate value of 9.7% recommended. A recent ENSDF library (ENSDF, June 2020) published just prior to our study recommends values of 12.7% and 10.4% for the 283 keV and 656 keV γ-ray intensities respectively.

The evaluated cross section in Fig. 8 was primarily based on experimental data from Takács et al. (Takács et al., 1997, 2001, 2007). Communication with the author (Takács, 2020) indicated that the 656 keV γ ray was used in these measurements to avoid room background in-

fluences at 283 keV. Hence, it is likely that the evaluated cross section in this energy region is incorrect by the same factor of 11%.

Therefore, to calculate integrated beam currents using Eq. 4, we used the revised 656 keV intensity of 9.7% (Bleuel et al., 2021) and correspondingly increased the ^{nat}Ni(d,x)^{61}Cu cross section by the ratio of the previous evaluated intensity to the revised value, from 23.3 mb to 24.9 mb interpolated at 15.6 MeV. These are compared to the charge collected from the target for each experiment in Tab. 2. Of course, a comparison could not be made for Exp. 4, in which no nickel attenuation foils were used. In each case, the charge calculated in this way from both γ rays agreed within 3-6%, with that of the charge collected from the electrically-isolated target.

Due to the potential error in the published ^{nat}Ni(d,x)^{61}Cu cross section and for consistency with Exp. 4, which lacked a nickel monitor, the ^{nat}Ar(d,x)^{41}Ar cross sections were calculated only from the measured charge collected from the electrically-isolated beam pipe, with the ^{61}Cu production used only for confirmation.

3.4. Calculation of Cross Section

Applying a more generalized version of Eq. 4 and rearranging terms, the cross section, σ, for the ^{40}Ar(d,p)^{41}Ar reaction is calculated,

$$\sigma = \frac{C\lambda A_{Ar}q_d\Delta t_i e^{\lambda\Delta t_{dk}}}{\rho_{Ar}f_{40}N_AQ\epsilon f_\ell\mathscr{I}_\gamma(1-e^{-\lambda\Delta t_c})(1-e^{-\lambda\Delta t_i})}, \quad (5)$$

where λ is the decay constant of ^{41}Ar, A_{Ar} is the atomic weight of ^{nat}Ar, q_d is the charge per deuteron (1.602 x 10^{-19} C), Δt_i is the irradiation time, ρ_{Ar} is the areal density of the argon gas in g/cm^2, f_{40} is the weight fraction of ^{40}Ar in natural argon, 0.99035(25), N_A is Avogadro's number, Q is the charge collected from the target assembly for each experiment, ϵ is the efficiency calculated in Sec. 3.2 of the HPGe detector to detect the 1293.64 keV characteristic γ ray of ^{41}Ar decay emitted from the volumetric gas source, f_ℓ is the detector live time fraction, $\mathscr{I}_\gamma$ is the intensity (0.9916) (Nesaraja and McCutchan, 2016) of the 1293.64 keV γ ray per decay of ^{41}Ar, Δt_c is the time over which the gas canister was counted, and Δt_{dk} is the time elapsed between the end of the experiment and the start of the count.

4. Results

The cross sections for the ^{40}Ar(d,p)^{41}Ar reaction for Exp. 1-4 were determined, respectively, as 351(12), 354(12), 355(12), and 338(12) mb. Measurements from the two experiments (Exp. 1 and 3) which produced the same average deuteron energy (5.5 MeV) were very close, well within 1σ uncertainty, lending confidence to the repeatability of the experiments. These cross sections are shown, along with those of Engle et al. (2012) and

the TENDL-2019 (Koning et al., 2019) evaluated cross section library, in Fig. 9. At 5.5 MeV, the cross sections of Exp. 1 and 3 were averaged in this plot, as was the error bar as each value's uncertainty was nearly identical and dominated by the same systematics.
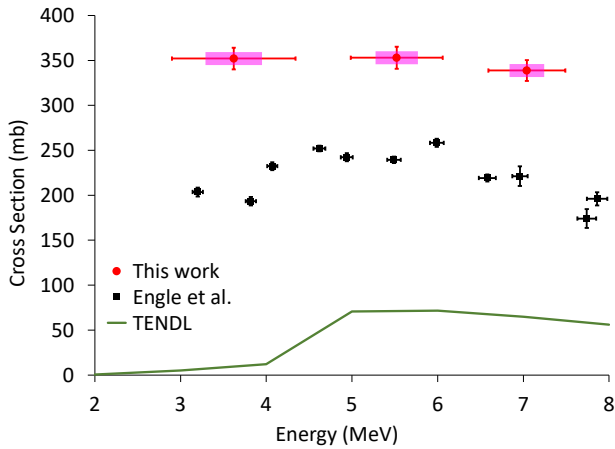

Figure 9: (Color online) Experimental cross sections from this work (red circles), Engle et al. (2012) (black squares), and TENDL (Koning et al., 2019) for the ^{40}Ar(d,p)^{41}Ar reaction. Magenta bands show the beam spread from energy straggling (height is arbitrary). Error bars of Engle data reflect only statistical uncertainty; systematic uncertainty was estimated at "less than 9%."

5. Discussion

A striking feature of Fig. 9 is the large difference between the cross section measurements obtained in this work and that of Engle et al. (2012). While both sets of experiments showed a relatively minor dependence on the cross section with energy (between 3-8 MeV), we observed about a 40% overall higher magnitude. The explanation for such a marked difference is not known, but may be due to a variety of factors. The previous experiment was optimized for measurement of chlorine isotopes rather than argon (Engle, 2017) and it is possible that the geometric efficiency for argon detection was not adequately known. Their argon gas volume was a long cylinder irradiated and measured perpendicular to the axis through a thin aluminum window. They assumed that chlorine would adhere to a metallic surface and be easily characterized as a point source while argon diffused into various cell components in a complicated and time-dependent manner. Furthermore, it was acknowledged that the higher beam current (200-600 nA) of the Engle et al. (2012) measurement would lead to target heating, effectively thinning the gas volume and lowering their measured cross section, though this was estimated to be a less than 6% effect. Due to the marked differences in results, another independent measurement is highly desirable.

Both experimental datasets are significant factors of 3-5 times higher than that of the TENDL library at energies above ∼5 MeV and orders of magnitude higher at

lower energies. A systematic sensitivity study was performed with the TALYS code (Koning et al., 2008), used to generate the TENDL library. Parameters were varied from the defaults through available optical, level density, and photon strength models. The generated cross section at its maximum value (5-6 MeV) never exceeded 100 mb, vastly lower than the differences in both measured values. For this reason, we do not recommend use of the TENDL library or any TALYS calculation for deuteron reactions in this mass region. Engle et al. (2012) produced a better absolute magnitude comparison with theoretical models using the ALICE-ASH code, though with less success in relative shape.

As previously noted, our measurements were optimized for accuracy and precision of the cross section measurement over the determination of deuteron energy, reflected in the large horizontal error bars in Fig. 9. The nearly energy-independent cross section over the energy range of 3 to 7 MeV facilitates the primary motivation of this study: the determination of the potential activation and associated radiation hazard of a deuteron beam stopping volume of argon gas circulated into an unshielded storage tank on the roof of a building. For a facility safety assessment (Anderson, 2016), a 7.5 MeV beam of 400 μA average current was assumed, with the entire beam stopping in a 3-atm argon target. This conservatively exceeds the expected operating conditions of a 300 μA, 7.07 MeV beam stopping in argon after slowing through 4 cm of 3 atm D_2 gas. Using interpolated energy loss data from SRIM to obtain a pathlength-weighted energy spectrum over the argon gas volume, along with TENDL cross section data, it was estimated that activities of 3.4×10^9 and 1.05×10^{11} Bq would be produced, respectively for a 5 min or 8 hour irradiation time. These correspond to respective dose rates, assuming all the gas is collected at a point source, of 0.59 and 18 rem/hr at 30 cm from the source.

As seen in Fig. 9, our measurements exceed the TENDL prediction by a factor of approximately five above 5 MeV and over an order of magnitude at lower energy. Using the same method, substituting our measured cross sections over the range of 7.5 MeV down to 2.5 MeV (where TENDL predicts an order of magnitude drop in cross section), activities of 2.5×10^{10} and 7.7×10^{11} Bq were obtained, respectively for a 5 min or 8 hour irradiation time. At 30 cm from a conservatively-assumed point source, this corresponded to 4.3 and 132 rem/hr, respectively. Following an 8-hour irradiation, a high radiation area (>100 mrem/hr) exists within a distance of about 11 m of an unshielded gas storage tank and a radiation area (>5 mrem/hr) exists within 49 m.

Obviously, this would produce a markedly significant radiation hazard, requiring an unreasonable restricted area for an unshielded gas storage tank. For this reason, significant shielding beyond that at the current facility is necessary. Otherwise, an alternative stopping gas such as krypton (which would require similar assessment), or a high-Z solid target (presuming heating challenges can be

7

addressed) like tungsten or tantalum, is recommended.

6. Summary

We have measured the ^{40}Ar(d,p)^{41}Ar cross section using an activation method at average energies of 3.6(7), 5.5(5), and 7.0(5) MeV and found them to be, respectively, 351(12), 355(12), and 338(12) mb. While the energy uncertainties and spread were considerable, the cross section is not observed to have a strong dependence on energy in this region. These values are about 40% larger than previously measured and almost an order of magnitude larger than the theoretical predictions of the TENDL library.

Acknowledgements

Anderson, S., 2016. personal communication.

Bleuel, D. L., Bernstein, L. A., Marsh, R. A., Morrell, J. T., Rusnak, B., Voyles, A. S., 2021. Precision measurement of relative γ-ray intensities from the decay of ^{61}Cu. Applied Radiation and Isotopes 170, 109625.
URL https://www.sciencedirect.com/science/article/pii/S0969804321000385

Engle, J., 2017. personal communication.

Engle, J. W., Severin, G. W., Barnhart, T. E., Knutson, L. D., Nickles, R. J., 2012. Cross sections of the ^{36}Ar(d,α)^{34m}Cl, ^{40}Ar(d,α)^{38}Cl, and ^{40}Ar(d,p)^{41}Ar nuclear reactions below 8.4 MeV. Applied Radiation and Isotopes 70 (2), 355–359.
URL https://www.sciencedirect.com/science/article/pii/S096980431100491X

ENSDF, June 2020. ENSDF document available from the National Nuclear Data Center ^{61}Cu EC decay dataset.
URL www.nndc.bnl.gov/ensdf/

Fitzpeaks, 2016.
URL http://www.jimfitz.co.uk/fitzpeak.htm

Hermanne, A., Ignatyuk, A. V., Capote, R., Carlson, B. V., Engle, J. W., Kellett, M. A., Kibédi, T., Kim, G., Kondev, F. G., Hussain, M., Lebeda, O., Luca, A., Nagai, Y., Naik, H., Nichols, A. L., Nortier, F. M., Suryanarayana, S. V., Takács, S., Tárkányi, F. T., Verpelli, M., 2018. Reference cross sections for charged-particle monitor reactions. Nuclear Data Sheets 148, 338 – 382.

Johnson, M. S., Anderson, S. G., Bleuel, D. L., Fitsos, P. J., Gibson, D., Hall, J. M., Marsh, R., Rusnak, B., Sain, J., 2017. Development of a high-brightness, quasi-monoenergetic neutron source for neutron imaging. Physics Procedia 90, 47–54, Conference on the Application of Accelerators in Research and Industry, CAARI 2016, 30 October – 4 November 2016, Ft. Worth, TX, USA.
URL https://www.sciencedirect.com/science/article/pii/S1875389217301773

Knoll, G. F., 1989. Radiation detection and measurement / Glenn F. Knoll, 2nd Edition. Wiley New York.

Koning, A. J., Hilaire, S., Duijvestijn, M. C., 2008. TALYS-1.0. Proceedings of the 2007 International Conference on Nuclear Data for Science and Technology - ND 2007, 211–214.

Koning, A. J., Rochman, D., Sublet, J.-C., Dzysiuk, N., Fleming, M., van der Marck, S., 2019. TENDL: Complete nuclear data library for innovative nuclear science and technology. Nuclear Data Sheets 155, 1–55.

Nesaraja, C. D., McCutchan, E. A., 3 2016. Nuclear data sheets for A = 41. Nuclear Data Sheets 133 (C).

Ninemire, B., 2016. personal communication.

Nuclear Wallet Cards, September 2019.
URL https://www.nndc.bnl.gov/wallet/wallet11.pdf

Ratkiewicz, A., Berzak Hopkins, L., Bleuel, D. L., Bernstein, L. A., van Bibber, K., Cassata, W. S., Goldblum, B. L., Siem, S., Velsko, C. A., Wiedeking, M., Yeamans, C. B., 2016. A recoverable gas-cell diagnostic for the National Ignition Facility. Review of Scientific Instruments 87 (11), 11D825.

Takács, S., 2020. personal communication.

Takács, S., Sonck, M., Azzam, A., Hermanne, A., Tárkányi, F., 1997. Activation cross section measurements of deuteron induced reactions on ^{nat}Ni with special reference to beam monitoring and production of for ^{61}Cu medical purpose. Radiochimica Acta 76 (1-2), 15–24.

Takács, S., Szelecsényi, F., Tárkányi, F., Sonck, M., Hermanne, A., Shubin, Y., Dityuk, A., Mustafa, M. G., Youxiang, Z., 2001. New cross-sections and intercomparison of deuteron monitor reactions on Al, Ti, Fe, Ni and Cu. Nuclear Instruments and Methods in Physics Research Section B: Beam Interactions with Materials and Atoms 174 (3), 235–258.

Takács, S., Tárkányi, F., Király, B., Hermanne, A., Sonck, M., 2007. Evaluated activation cross sections of longer-lived radionuclides produced by deuteron induced reactions on natural nickel. Nuclear Instruments and Methods in Physics Research Section B: Beam Interactions with Materials and Atoms 260 (2), 495–507.

Ziegler, J. F., Ziegler, M. D., Biersack, J. P., 2010. SRIM – the stopping and range of ions in matter (2010). Nuclear Instruments and Methods in Physics Research Section B: Beam Interactions with Materials and Atoms 268 (11), 1818–1823.
URL http://www.srim.org

Zuber, K., Singh, B., 2015. Nuclear data sheets for A = 61. Nuclear Data Sheets 125, 1–200.

- We measured the ^{41}Ar(d,p)^{40}Ar cross section at 3.6, 5.5 and 7.0 MeV using an activation method.
- Our measured cross section was about 40% higher than a previous measurement and nearly an order of magnitude higher than the TENDL library.
- Without significant shielding, argon is not recommended as a deuteron beam stopping medium.

Declaration of interests

☒ The authors declare that they have no known competing financial interests or personal relationships that could have appeared to influence the work reported in this paper.

☐ The authors declare the following financial interests/personal relationships which may be considered as potential competing interests: